*Small Structures*

small structures

www.small-structures.com

RESEARCH ARTICLE OPEN ACCESS

# Electrochemical DNA-Based Biosensors for In Vivo Quantification of a Therapeutic Protein

Alejandro Chamorro-Garcia[1] | Lisa Fetter[2,3] | Nicole A. Emmons[4] | Myriam Alfonsini[1] | Elisa Paialunga[1] | Bettina Glahn-Martínez[5] | Elena Benito-Peña[5] | Giovanni Valenti[6] | Alessandro Porchetta[1] | Tod E. Kippin[3,4,7] | Kevin W. Plaxco[2,3] | Andrea Idili[1]

[1]Department of Chemical Sciences and Technologies, University of Rome Tor Vergata, Rome, Italy | [2]Department of Chemistry and Biochemistry, University of California Santa Barbara, Santa Barbara, California, USA | [3]Interdepartmental Program in Quantitative Biology, University of California Santa Barbara, Santa Barbara, California, USA | [4]Department of Psychological and Brain Sciences, University of California Santa Barbara, Santa Barbara, California, USA | [5]Department of Analytical Chemistry, Faculty of Chemistry, Universidad Complutense de Madrid, Madrid, Spain | [6]Department of Chemistry "Giacomo Ciamician", Alma Mater Studiorum – University of Bologna, Bologna, Italy | [7]Department of Molecular, Cellular, and Developmental Biology, University of California Santa Barbara, Santa Barbara, California, USA

**Correspondence:** Andrea Idili (andrea.idili@uniroma2.it)

**Received:** 15 December 2025 | **Revised:** 24 June 2026 | **Accepted:** 29 June 2026

**Keywords:** continuous molecular monitoring | electrochemical aptamer-based sensors | implantable biosensors | point-of-care testing | precision medicine | real-time pharmacokinetics | structure-switching aptamers

## ABSTRACT

Inter-subject pharmacokinetic variability limits the clinical effectiveness of many "biologics", including monoclonal antibody drugs. This issue can be addressed through therapeutic drug monitoring (TDM), in which clinicians tailor dosing to individual patients based on measured plasma drug concentrations. In practice, TDM is inconvenient because current methods for quantifying protein drugs in blood are labor-intensive and expensive. In response, here we present an electrochemical DNA-based biosensor that addresses this issue by enabling rapid, reagentless measurement of plasma concentrations of the antibody drug trastuzumab. The approach supports real-time, in vivo monitoring in living animals (rats). Specifically, we have systematically compared two distinct sensing architectures, a DNA scaffold sensor and an electrochemical aptamer-based sensor, before developing an optimized sensor in the latter class that, when challenged in undiluted whole blood, can measure over the entire clinical range of the drug. When implanted in animals, the sensor successfully tracks in vivo drug concentrations and clearly visualizes differences in drug exposure between individual rats following intravenous infusion. Given the ability to generalize EAB sensors to almost any target of interest, this work illustrates a powerful new tool to guide real-time dosing of biologic therapeutics, enabling personalized treatments of this increasingly important class of drugs.

## 1 | Introduction

While therapeutic monoclonal antibodies as biologically derived protein drugs have revolutionized the treatment of numerous diseases [1–4], their clinical efficacy is often unpredictable [5, 6]. For example, immune checkpoint inhibitors, a class of antibody drugs used in immunotherapy, achieve meaningful prolonged survival in only a limited subset of cancer types, with 5-year survival rates reaching a maximum of 30%–40% [7]. This variability arises from a combination of anthropometric and biological factors [8] but is often driven by differences in drug exposure [9]. Specifically, patients on standard dosing regimens frequently fail to reach optimal in vivo drug concentrations [10]. Such discrepancies can lead to under-dosing, reducing therapeutic benefit, or over-dosing, which increases the risk of toxicity, promotes the formation of neutralizing, anti-drug antibodies (ADA), and drives up treatment costs [8, 11].

This is an open access article under the terms of the Creative Commons Attribution License, which permits use, distribution and reproduction in any medium, provided the original work is properly cited.

© 2026 The Author(s). *Small Structures* published by Wiley-VCH GmbH.

While poor control over the patient's actual drug exposure presents a significant challenge, this can be solved by performing therapeutic drug monitoring (TDM), in which patient-specific pharmacokinetics are measured, enabling the high-precision individualization of dosing (Figure 1A) [16]. Current methods for quantifying the plasma concentrations of specific antibodies, however, rely on centralized laboratory immunoassays (e.g., ELISAs, ECLIAs [17–19], or cell-based mobility shift assays [20]) all of which require blood draws, specialized equipment, and long turnaround times [21]. The logistical burdens associated with this render TDM costly and inconvenient [22], consequently limiting how frequently it is performed. In routine clinical practice, for example, drug concentrations are typical measured only at sparse time points, most often as trough samples collected immediately prior to subsequent treatment cycles and occasionally 2–8 weeks post-treatment, leading to temporal resolution that is insufficient to ensure that drug concentrations stably remain within the therapeutic range [12]. In response, recent studies have explored localized (e.g., lesion-specific) in vivo drug sensing aimed at monitoring drug activity within defined tissue microenvironments [13]. While such approaches provide valuable spatial insights, however, they do not address the distinct challenge of continuously quantifying circulating systemic drug concentrations, which remains central to TDM [14]. Here, however, we have developed and compared two distinct electrochemical DNA-based (eDNA) sensors for the detection of an antibody drug: a DNA scaffold sensor [15] (Figure 1B) and an electrochemical aptamer-based (EAB) sensor (Figure 1C) [23, 24], both directed against the antibody drug trastuzumab. This antibody drug, which is a cornerstone treatment for HER2-positive cancers, suffers from both cardiotoxic side effects and variable clearance [25], emphasizing the value of adding TDM to its clinical use. Our technology offers a transformative tool for personalizing biologic therapies, improving patient outcomes, and advancing our understanding of antibody drugs pharmacokinetics.

## 2 | Results and Discussion

### 2.1 | Design and Characterization of the Trastuzumab-Binding Aptamer

As the recognition element in our sensors, we have employed an existing DNA aptamer that binds trastuzumab with clinically-relevant affinity and specificity [26]. Specifically, we used a 32-base truncation of this aptamer (here called "Parent Trunc1") that binds trastuzumab with the same affinity as the 76-base as-selected aptamer sequence. This Parent Trunc1 is thought to fold into a stem-loop conformation flanked by a 7-base-pair stem, within which nucleotides in the loop region directly interact with the antigen-binding fragment (Fab) of the target (Figure S1). To validate the binding and specificity of this aptamer, we modified its 5′-end with the fluorophore cyanine 5 and used microscale

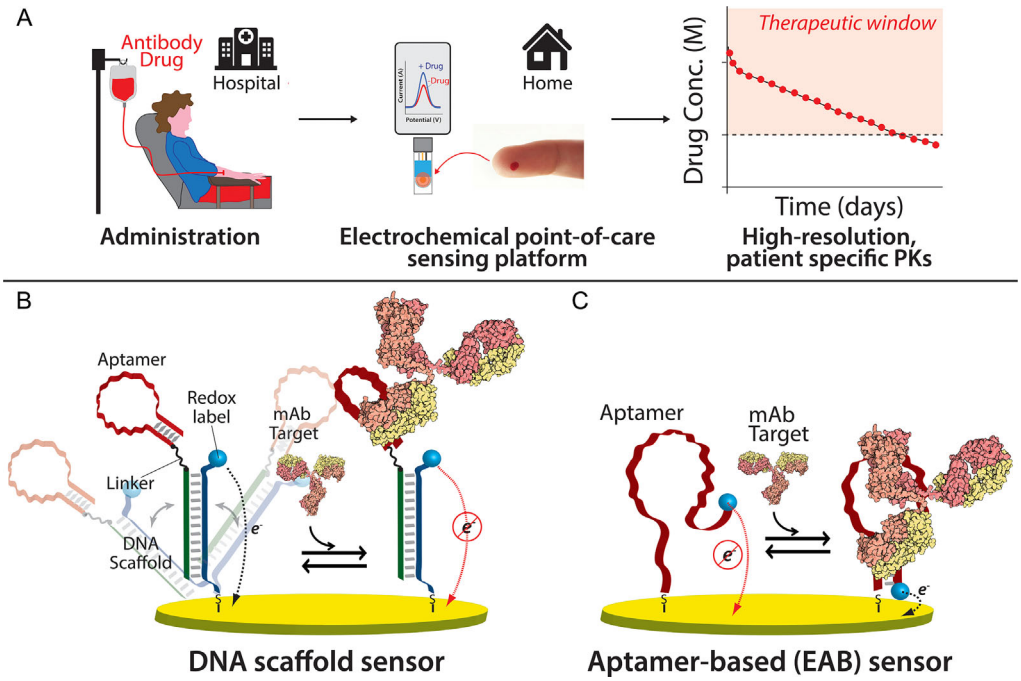



**FIGURE 1** | (A) Current clinical approaches for surveilling the clinical outcome rely on tedious, costly processes typically requiring trained personnel and specialized facilities. Given these technical challenges, antibody drug-based therapies are not commonly monitored, reducing the impact or efficiency of the therapy in the patient [12]. The implementation of a convenient, single-step test that relies on finger-prick blood samples or on small noninvasive wearable patches would facilitate patient management by enabling personalized treatment strategies. To measure trastuzumab, we have developed two distinct DNA-based sensing architectures. (B) The first is an electrochemical DNA scaffold platform [15]. This is a double-stranded DNA structure appended with a trastuzumab-specific aptamer and a redox reporter (i.e., methylene blue) anchored to the electrode surface. The target binding produces a steric hindrance affecting the redox reporter's electron transfer efficiency and consequently decreases the electrochemical signal. This phenomenon quantitatively correlates with the drug's concentration. (C) The second platform is an electrochemical aptamer-based (EAB) sensor [23, 24]. This approach uses an aptamer tethered to a gold electrode through a thiol group on one end and labeled with a redox reporter (i.e., methylene blue) on the other. Upon target binding, a conformational change shifts the reporter's proximity to the electrode, inducing a measurable change in the electrochemical signal.



26884062, 2026, 7, Downloaded from https://onlinelibrary.wiley.com/doi/10.1002/sstr.70539 by CochraneItalia, Wiley Online Library on [22/10/2026]. See the Terms and Conditions (https://onlinelibrary.wiley.com/terms-and-conditions) on Wiley Online Library for rules of use; OA articles are governed by the applicable Creative Commons License

thermophoresis (MST) and measured its affinity [27, 28]. Using this approach, we found that Parent Trunc1 binds trastuzumab with a dissociation constant ($K_D$) of 5.7 ± 1.6 nM (Figure S2), a value that agrees with prior studies [26]. (Unless otherwise stated, errors for $K_D$ values represent estimated standard errors derived from a Langmuir binding model fit). The aptamer is also specific for Trastuzumab, as it does not detectably bind to other antibody drugs (i.e., bevacizumab and rituximab) or to a mixture of human IgGs (Figure S3).

## 2.2 | DNA Scaffold Sensors

As our first approach toward converting the trastuzumab-binding aptamer into a sensor, we explored a "DNA scaffold sensor" architecture [15, 29]. In this, the binding of the large molecular target to a receptor sterically hinders the motion of a short, electrode-bound, redox-reporter-modified double-stranded DNA structure (the "scaffold"), reducing the rate of electron transfer, an effect that can be easily detected using square wave voltammetry (SWV) [29, 30] (Figure 1B). Given this signal transduction mechanism, scaffold sensors eliminate the need to re-engineer the recognition aptamer into a structure switching receptor (Figure 1C). Building on this concept, here we designed a DNA scaffold sensor architecture consisting of two DNA elements. The first, the anchor strand, is a 21-base, single strand of DNA attached to the surface via a 5′-thiol group and containing a methylene blue redox reporter at its 3′-end. The second, the recognition strand, incorporates the target-recognizing aptamer attached to a linear sequence complementary to the anchor strand that causes the two to form a 21-base-pair double helix adjacent to the surface attachment with the aptamer on the distal end of the sensor. Because the flexibility of the connection between the recognition element to the double-stranded region is known to affect the signaling of such sensors [29], here we designed and tested variants differing in this linker: one with no linker, one with a flexible poly-thymine linker, and one with a polyethylene glycol (PEG) linker comprised of 3 molecules of ethylene oxide units (Figure 2A).

The DNA-scaffold sensors respond to the presence of trastuzumab, albeit with quite low signal gain (the relative change in signal upon saturation with the target). To demonstrate this, we immobilized the three sensor variants on gold electrodes

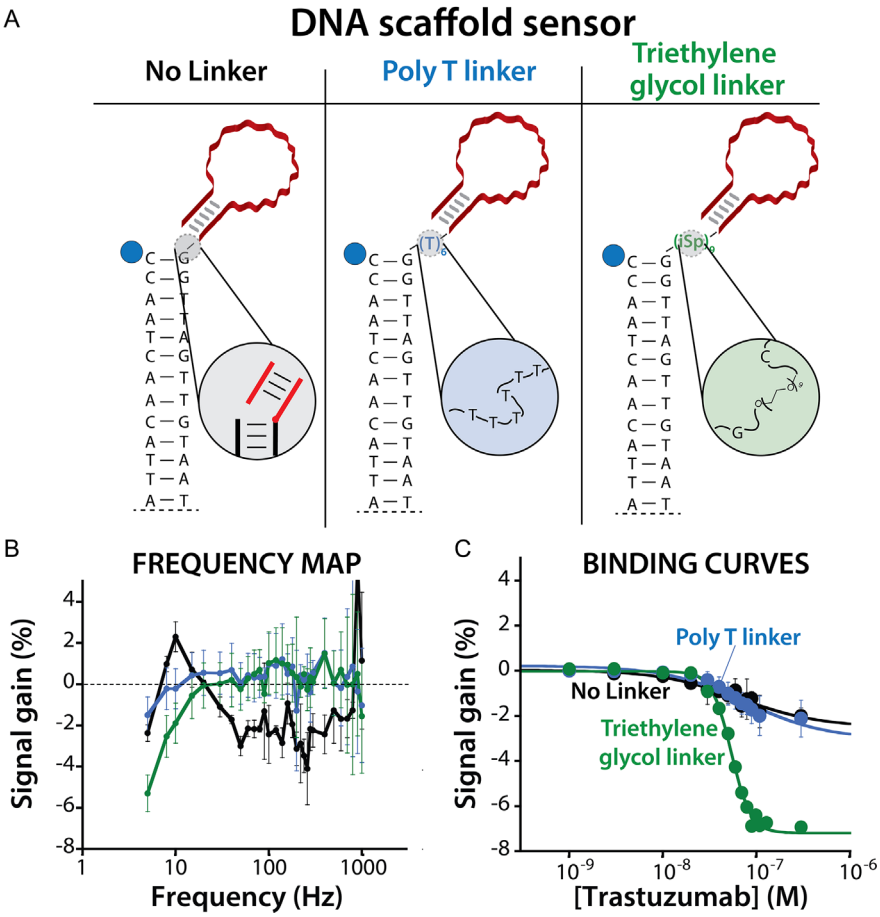



**FIGURE 2** | Schematic of the electrochemical DNA scaffold sensor. Three different linkers were compared to connect the recognition domain (the aptamer sequence, shown in red) and the scaffold region (the redox and attachment group): no linker (A left), a poly T of six thymine bases (A center), and a triethylene glycol linker (A right). (B) The frequency dependence of the gain for the three linker variants was studied by plotting the signal gain as a function of the square wave voltammetry (SWV) frequency, both in the absence and in the presence of the target (300 nM trastuzumab). (C) Dose-response curves for the three linker architectures were generated by challenging the sensors with increasing concentrations of trastuzumab and the electrochemical signal collected at their optimal SWV frequency (defined as the frequency that produced the highest signal gain in panel B). The data show that these DNA-scaffold sensors achieve only modest performance, with the best of these, the PEG linker variant, exhibiting only −7% gain. The error bars reflect standard deviations derived from at least three sensors fabricated independently.



26884062, 2026, 7, Downloaded from https://onlinelibrary.wiley.com/doi/10.1002/sstr.70539 by CochraneItalia, Wiley Online Library on [22/10/2026]. See the Terms and Conditions (https://onlinelibrary.wiley.com/terms-and-conditions) on Wiley Online Library for rules of use; OA articles are governed by the applicable Creative Commons License

and performed in vitro measurements in a simple buffer solution. While initial tests confirmed all sensors responded to trastuzumab across SWV frequencies ranging from 5 to 1000 Hz [29, 31] (Figure 2B), their dose–response curves revealed only modest performance (Figure 2C). Specifically, the no-linker and poly-thymine-linker variants displayed poor signal gain (−2.5% ± 0.3% and −3.3% ± 0.3%, respectively). (Unless otherwise stated, reported errors for signal gain represent estimated standard error derived from a Langmuir binding model fit). The PEG-linker variant, in contrast, yielded somewhat better performance, but even this reached a maximum signal gain of only −7.2% ± 0.2%. The three sensors exhibited dissociation constants ($K_D$) of 66 ± 22, 77 ± 25, and 54 ± 2 nM, respectively, which, as expected (because they use the same recognition element), are within error of one another (Table S1). With this performance, none of these sensors are suitable for monitoring clinically relevant trastuzumab concentrations [32].

### 2.3 | Electrochemical Aptamer-Based (EAB) Sensors

With the aim of obtaining higher gain and thus a sensor architecture better suited for clinical use [14], we next turned to the EAB platform. EAB sensors are comprised of an aptamer immobilized on a gold electrode and labeled with methylene blue (Figure 1C) [23]. In this platform, the aptamer undergoes a binding-induced conformational change, which alters the position of a tethered redox reporter and, therefore, the efficiency with which it exchanges electrons with the interrogating electrode [33, 34]. This mechanism generates an easily measurable electrochemical signal and offers several key advantages, including intrinsic resistance to non-specific adsorption, rapid interrogation times, and compatibility with in vivo deployment [35]. Harnessing these advantages, however, requires an aptamer specifically engineered to produce a large structural change while maintaining appropriate affinity for its target [36]. To adapt the parent trastuzumab aptamer, which was selected for its high affinity rather than for structure switching, to a solution-based fluorescence assay (rather than electrochemical detection demonstrated here), the original authors truncated it to create a structure-switching variant ("Parent Trunc1") [26]. To adapt this truncation into an EAB platform, we characterized this and 3 additional variants (Figures 3A and S1). These included 2 variants predicted to be less stable (Figure S1) ("Trunc2" and "Trunc2(TA)") and one predicted to be more stable (by extending the stem; "Trunc1 Stem"; Figure 3A). To incorporate these variants into the electrochemical platform, we modified each by adding a thiol group and a methylene blue redox reporter to the 5′ and 3′ ends, respectively (Figure 3A).

When deployed as EAB sensors, the parent truncation and our three additional engineered variants all responded in a "signal-on" manner to trastuzumab, but with significant differences in performance. Specifically, the destabilized Trunc2 and Trunc2(TA) variants exhibited notably higher signal gain (47.4% ± 1.6% and 18.7% ± 1.0%, respectively) than the other two variants (Figure 3B and Table S2). We hypothesize that the superior signal gain of Trunc2 and Trunc2(TA) arises because the destabilization of their stem-loop conformation shifts a larger fraction of the target-free aptamers into the flexible, unfolded state (Figure S4), thereby increasing the signal change seen at saturating target concentration. Despite their both being designed to be destabilized, however, the gains of Trunc2 and Trunc2(TA) differ significantly. We believe this disparity stems from the fact that each modification has a specific structural impact on the binding pocket. Consistent with this, molecular dynamics simulations and mutational analyses have identified nucleotides T24 and G25 as key contributors to trastuzumab binding [26]. Given this, we hypothesize that in Trunc2, destabilization occurs while preserving GC pairing adjacent to this binding region, maintaining local structural pre-organization and enabling a more significant conformational rearrangement upon target binding. In contrast, substitution with TA pairs in Trunc2(TA) may increase local flexibility near the binding interface, potentially weakening conformational coupling between target binding and reporter displacement. Although further structural studies are required to confirm this mechanism, these observations suggest that signal gain depends not only on thermodynamic destabilization but also on the structural context of the binding interface. Consistent with this, the dissociation constants of the sensors are, at 23 ± 9 nM for Parent Trunc1, 29.1 ± 0.7 nM for Trunc1 stem, 40 ± 6 nM for Trunc2, and 21 ± 5 nM for Trunc2(TA), consistent with the claim that the Trunc2 variant is the most destabilized (Figure 3C and Table S2). Given the gains and affinities of the various sensors, the Trunc2 variant offers the best overall analytical performance.

The trastuzumab-detecting EAB sensor supports quantitative, specific measurement of its target directly in undiluted whole blood. Under these conditions, the Trunc2 sensor produced a gain of 74% ± 3% (Figures 4A and S5), which is notably higher than the gain we observed in simple buffered solution. Conversely, the sensor's affinity is reduced ∼2-fold in blood ($K_D = 106 \pm 18$ nM), suggesting that both effects are due to reduced thermodynamic stability of the aptamer in blood (i.e., more of the aptamers are unfolded in the absence of target, leading to higher gain but poorer affinity). Despite this shift, the sensor's useful dynamic range still overlaps with the >130 nM clinical range of the drug (Figure 4A) [39]. The sensor is also specific. To assess this in a clinically relevant matrix, we challenged the sensor with abundant blood proteins and structurally related antibodies that could potentially interfere with target recognition. The sensor exhibited negligible signal change when exposed to bovine serum albumin (BSA) and bovine IgG (Figure 4B, gray and brown curves), which serve as representative high-abundance serum proteins. The sensor likewise exhibited no detectable response when challenged with human IgGs at their ∼10 μM physiological concentration in blood [40] (Figure 4C, orange curve).

A unique feature of EAB sensors is their capacity to perform high-frequency, real-time monitoring directly in biological fluids. Key to this is the rapid equilibration of the sensor: time-resolved measurements reveal that, in undiluted blood, the Trunc2 sensor equilibrates with a time constant of 0.7 ± 0.2 $min^{-1}$ at 1 μM target (Figure 4D). This rapid binding enables dynamic tracking of trastuzumab levels in whole blood. To demonstrate this, we continuously monitored the sensor signal in whole blood at 25 and 37 °C (Figure S6), collecting data every 25 s (Figure 4E,F). After a stable baseline was established, sequential additions of 100 nM and 1 μM trastuzumab produced rapid increases in sensor output. Consistent with the aptamer's high affinity, however, the sensor exhibits a slow dissociation rate (0.03 ± 0.01 $min^{-1}$) when returned to a target-free sample (Figure S7), indicating that it is not fully reversible on short timescales. Nevertheless, this behavior is



26884062, 2026, 7, Downloaded from https://onlinelibrary.wiley.com/doi/10.1002/sstr.70539 by CochraneItalia, Wiley Online Library on [22/10/2026]. See the Terms and Conditions (https://onlinelibrary.wiley.com/terms-and-conditions) on Wiley Online Library for rules of use; OA articles are governed by the applicable Creative Commons License

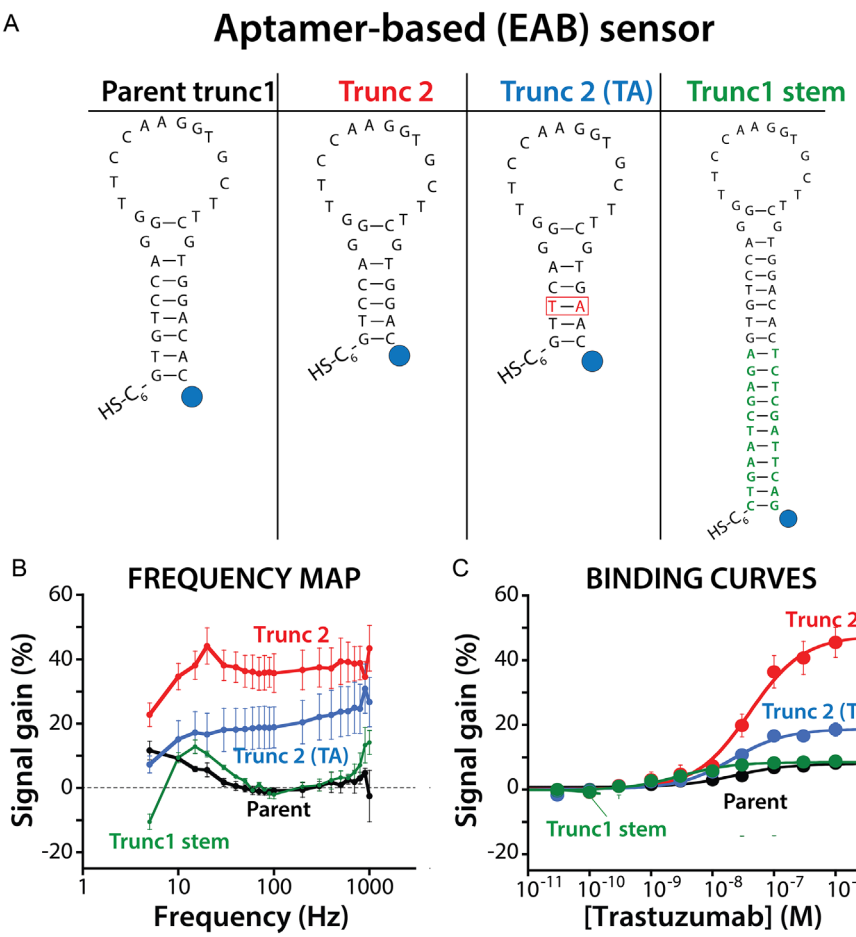



**FIGURE 3** | We tested four variants of the trastuzumab aptamer as electrochemical aptamer-based (EAB) sensors. (A) These variants were modified at their 3′ end with a methylene blue redox reporter and at their 5′ end with a thiol group to anchor the aptamer to the electrode surface. The first variant consisted of the original binding region of the selected aptamer (Parent Trunc 1) [26]. Trunc 2 presented a two-base deletion from the parent Trunc1; Trunc2(TA) presented the two-base base deletion and one substitution in the stem portion, CG in favor of TA; and Trunc1 stem consisted of the parent aptamer with a longer stem portion. (B) We first assessed the effect of square-wave frequency on the magnitude and sign (i.e., signal-on or signal-off) of each sensor's gain [37, 38]; for the four aptamer variants in absence and presence of the target (300 nM trastuzumab), being Trunc2 variant the one producing the highest signal changes. (C) The dose response of the four variants at increasing trastuzumab concentrations showed that Trunc 2 variant responded best in terms of signal gain. The error bars reflect standard deviations derived from at least three sensors fabricated independently.

compatible with TDM, as monoclonal antibody concentrations in patients change only gradually due to their slow physiological clearance (from days to weeks) [32, 41]. Consequently, the sensor could be effectively used to estimate drug concentrations at infrequent intervals (e.g., once per day), enabling practical point-of-care implementation for TDM applications [7, 22].

## 2.4 | Real-Time Measurement of Therapeutic Antibodies In Vivo

EAB sensors support high-frequency in vivo measurements [42, 43], suggesting that the Trunc2 sensor will similarly support such measurements. To explore this, we fabricated in vivo sensors by pairing a 200 µm diameter, 4 mm long gold working- electrode on which EAB was deposited with a 125 µm diameter, 5 mm long platinum counter-electrodes and a 125 µm, 5 mm long chloride-anodized silver reference electrodes (Figures 5A–C and S8A–D). We then electrochemically roughened the gold working electrode to increase its electroactive surface area. As previously demonstrated by scanning electron microscopy (SEM), this roughening protocol produces a nanostructured morphology characterized by needle-like features and the formation of a porous film on the gold surface [44]. Electrochemical analysis further confirms that this treatment increases the microscopic electroactive area. Specifically, cyclic voltammetry performed in sulfuric acid solutions reveals increased peak currents associated with the reduction of chemisorbed oxygen on gold (Figure S9), and higher capacitive current in working buffer (Figure S10a). Electrochemical impedance spectroscopy (EIS) performed in the presence of a ferri/ferrocyanide redox moiety also indicates that charge–transfer resistance is lower after the roughening procedure (Figure S10), which is consistent with an increase in the electroactive area of the electrode. Subsequent aptamer immobilization and mercaptohexanol passivation produce the expected increase in interfacial resistance, and cyclic voltammetry reveals the characteristic methylene blue redox peaks (Figures S10B and S11), confirming successful assembly of the electrochemical aptamer-based sensing interface. Together, these measurements validate each stage of



26884062, 2026, 7, Downloaded from https://onlinelibrary.wiley.com/doi/10.1002/sstr.70539 by CochraneItalia, Wiley Online Library on [22/10/2026]. See the Terms and Conditions (https://onlinelibrary.wiley.com/terms-and-conditions) on Wiley Online Library for rules of use; OA articles are governed by the applicable Creative Commons License

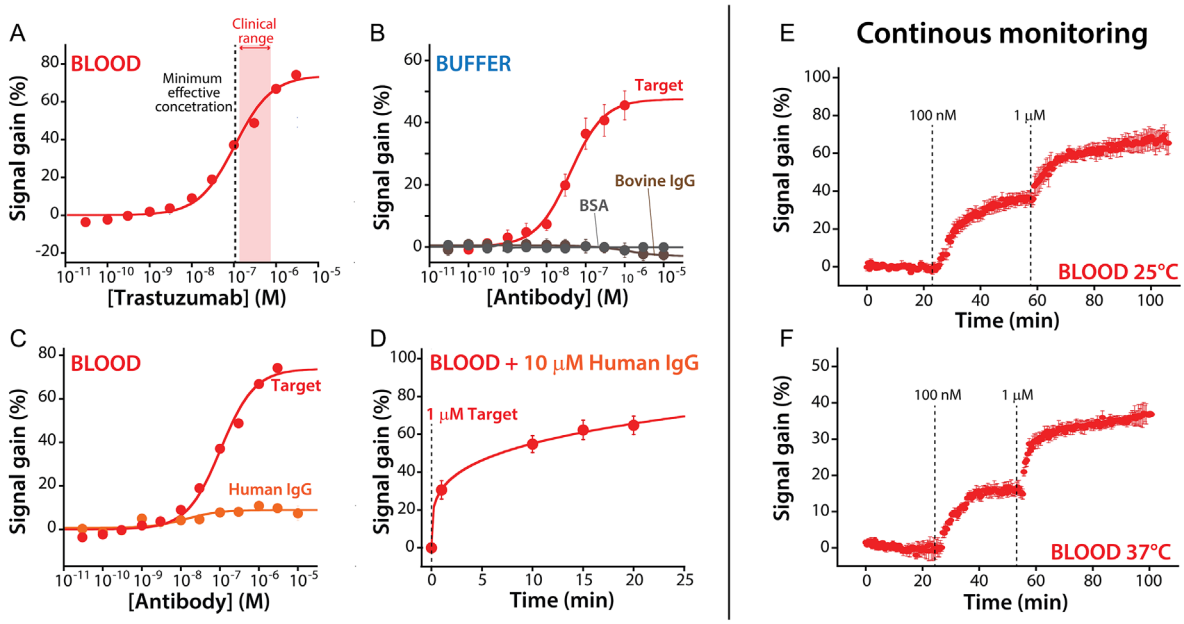



**FIGURE 4** | Electrochemical aptamer-based sensors (EAB sensors) for the different aptamer variants were tested in vitro in undiluted bovine whole blood, and the responses at the best performing of square wave voltammetry (SWV) frequencies were compared. (A) Trunc2 was selected as the best performing variant in whole blood. (B) Further characterizations included the specificity test against bovine IgGs and BSA at 25 °C in buffer solution. (C) The specificity test at 25 °C demonstrated that human IgGs did not interfere with the EAB sensor, thus validating its working capabilities in undiluted whole blood (D). Kinetic measurements of trastuzumab in the presence of a high concentration of human IgG (10 μM) demonstrate the sensor's capability to operate even at naturally occurring levels of interferents. (E,F) To evaluate the possibility of performing real-time, continuous monitoring of trastuzumab in blood, the response of an EAB sensor made with the Trunc 2 variant was studied over time, at both 25 °C (E) and 37 °C (F). The sensor successfully measured trastuzumab spiked at two different time points (20 and 50 min) demonstrating an equilibration time of just a few minutes. Note that the 1 μM addition was performed after the initial addition of 100 nM, thus, the second response reflects an incremental increase from an already partially bound state, which, due to the Langmuir binding isotherm of the aptamer, is smaller than the change associated with the first addition (A). Note that here the error bars reflect standard deviations derived from at least three independently fabricated sensors.

electrode fabrication while preserving efficient electron transfer at the sensing surface.

Once the sensor is fabricated, we encased it in a 22-gauge catheter (Figure S8E–G) to create a bundle small enough to insert into the jugular vein of an anesthetized Sprague–Dawley rat (Figures 5D and S8H). As the calibration matrix for these in vivo sensors we employed fresh, undiluted rat blood [45], finding that performance in this matrix is comparable to our earlier results obtained in bovine blood (Figure S8). A known challenge for in vivo electrochemical sensors, however, is the baseline drift arising from the degradation of the sensing surface during continuous electrochemical interrogation [46]. To overcome this, we implemented "kinetic differential measurements" (KDM) [35]. This method is based on the observation that signal-on and signal-off signals are generated by interrogating the sensor at a pair of SWV frequencies that drift together (Figure 5E). By subtracting the normalized peak currents observed at the signal-on (here, 200 Hz) and signal-off (here, 20 Hz) frequencies and then dividing the resulting difference by their average, we effectively remove the drift, thereby enabling accurate, in vivo determination of target concentration [35, 47, 48] with temporal resolution of 30 s (Figure 5F).

The Trunc2 sensor supports high-frequency, quantitative measurement of therapeutic antibody concentrations directly in vivo, establishing the first proof-of-concept for real-time monitoring of a monoclonal antibody drug in a living animal. For example, following an infusion of trastuzumab (2 mg/kg over 1 min), the sensor successfully tracked the increase in plasma concentration, over the course of 15 min, to a peak ($C_{max}$) of 84 ± 6 nM. This was followed by an initial slow decrease as the drug began to be distributed in the body (Figure 5G). Given the antibody's long half-life relative to the duration of our in vivo measurements (which were limited by animal welfare concerns), combined with the sensor's slow dissociation kinetics, our objective here was not to perform a formal pharmacokinetic analysis. Instead, this experiment provides a critical proof-of-concept by demonstrating for the first time that an electrochemical DNA-based sensor can directly track dynamic changes in therapeutic antibody concentration in vivo, and ultimately our Trunc2 EAB sensor can be used as a tool to study the pharmacokinetics of the antibody drug. We repeated the experiment with two additional animals, administering the same mass-adjusted dose (Figure 5H,I). The sensor revealed distinct concentration-time profiles for each animal, with notable differences in $C_{max}$, which ranged from 59 ± 6 to 148 ± 12 nM (Figure 5H,I). These $C_{max}$ values align well with values previously reported for rodent models, confirming that our sensor is capturing expected concentrations [49, 50]. The ability to directly visualize such clear differences between individuals, even without deriving formal pharmacokinetic parameters, powerfully illustrates the value of this sensing technology. This highlights the potential for real-time monitoring to reveal the



26884062, 2026, 7, Downloaded from https://onlinelibrary.wiley.com/doi/10.1002/sstr.70539 by CochraneItalia, Wiley Online Library on [22/10/2026]. See the Terms and Conditions (https://onlinelibrary.wiley.com/terms-and-conditions) on Wiley Online Library for rules of use; OA articles are governed by the applicable Creative Commons License

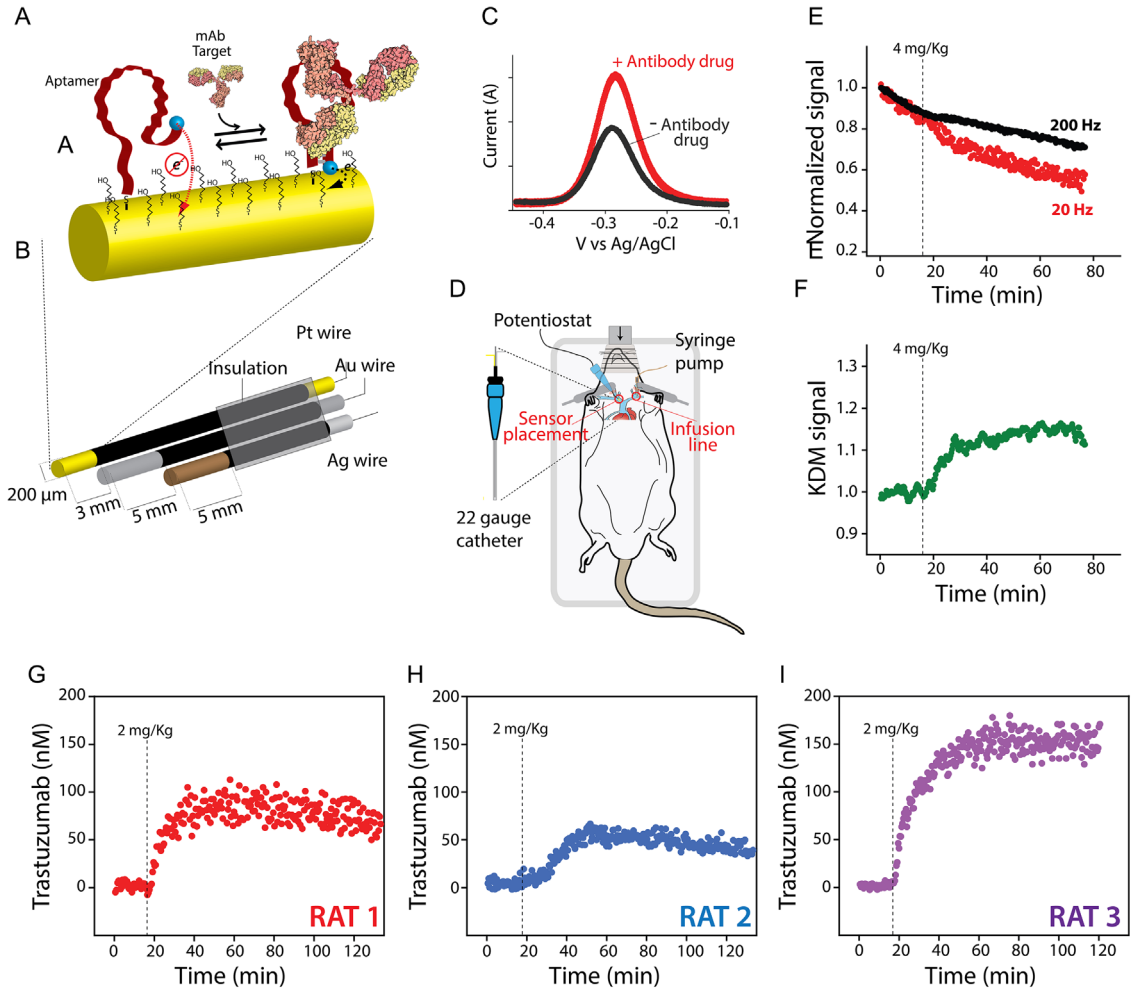



**FIGURE 5** | (A) The electrochemical aptamer-based sensors (EAB) sensing architecture that relies on an aptamer modified with a redox reporter tethered to a gold electrode. (B) This can be easily deployed on to a wire sensor platform, for in vivo applications. The sensor is constructed as an implantable probe featuring a 200 µm diameter gold working electrode bundled with platinum counter and Ag/AgCl reference electrodes. (C) Structural changes in the aptamer upon target binding alter the proximity of the redox reporter (here methylene blue) to the electrode surface, modulating the electron-transfer rate, which can be simply measured by square-wave voltammetry (SWV). (D) The compact, fully assembled probe is designed for intravenous placement into the jugular vein of a rat via a standard 22-gauge guide catheter. (E) Normalized signals collected in vivo at different square-wave frequencies (20 Hz, red; and 200 Hz, black) exhibit significant, correlated baseline drift. To correct that we used the kinetic differential measurement (KDM) approach, that relies on subtracting the normalized signals of two frequencies to produce a stable, drift-corrected output (F). that tracks the real-time plasma concentration of trastuzumab in an anesthetized rat following intravenous infusion. The EAB sensor provides a high-resolution view into the inter-subject variability of drug pharmacokinetics. Shown are the real-time plasma trastuzumab concentrations monitored in three separate anesthetized rats (G–I), each receiving an identical mass-adjusted intravenous dose (2 mg/kg). Of note, despite the standardized dosing, the drift-corrected sensor output reveals clear subject-to-subject differences in the resulting drug exposure profiles.

patient-specific drug responses that are obscured by the sparse sampling used in current clinical practice, paving the way for truly personalized dosing strategies.

## 3 | Conclusion

Here, we have developed a novel electrochemical aptamer-based sensor that enables real-time, high-frequency monitoring of the antibody drug trastuzumab, taking the sensing technology from initial in vitro concept to an in vivo demonstration. We have described a systematic bioengineering process, beginning with a head-to-head comparison of multiple variants of two distinct aptamer-based sensor architectures (a DNA scaffold sensor and an EAB sensor) and culminating in a rationally optimized EAB sensor that provides high gain, drift-free performance in whole blood. Finally, we also demonstrated the sensor's ability to continuously monitor drug concentration directly in living animals, a result that represents the first real-time, in vivo monitoring of a protein-based therapeutic target. This demonstrates the potential for continuous quantification of antibody drug concentration profiles following administration, and, consequently, the ability to capture inter-subject differences in drug exposure, which are fundamental challenges of personalized medicine that, until now, had only been tackled using costly, time consuming, low-time resolution, laboratory-based measurements.



26884062, 2026, 7, Downloaded from https://onlinelibrary.wiley.com/doi/10.1002/sstr.70539 by CochraneItalia, Wiley Online Library on [22/10/2026]. See the Terms and Conditions (https://onlinelibrary.wiley.com/terms-and-conditions) on Wiley Online Library for rules of use; OA articles are governed by the applicable Creative Commons License

Looking forward, the technology described here could produce a significant advance in precision medicine as applied to antibody-drug therapies. Specifically, the ability to monitor the plasma concentrations of such a drug rapidly and conveniently opens the door to personalized dosing regimens, where drug delivery can be adjusted instantly to maximize efficacy and minimize toxicity. The modularity of the EAB platform suggests that this approach could be readily adapted to a wide array of other therapeutic antibodies, peptides, and small-molecule drugs by simply exchanging the aptamer. This would herald a new era of personalized medicine.

While the present, in vivo study represents a proof-of-concept demonstration, long-term deployment of EAB sensors remains an important translational objective [42, 43, 51]. To this end, recent advances, including dual-frequency drift correction, antifouling surfaces, nanostructured electrodes, and improved aptamer chemistries (e.g., the use of non-natural nucleic acid backbones) have significantly extended sensor longevity [42, 43, 51, 52]. This said, a recent first-in-human study has already demonstrated the ability of wearable EAB-based microneedle patches to track a small molecule drug in the dermal interstitial fluid of humans for up to 24 h, highlighting the growing clinical feasibility of this platform [14]. Given this, we believe the antibody-sensing platform described here offers a realistic route toward extended in vivo monitoring of biologic therapeutics for clinical TDM.

## 4 | Materials and Methods

### 4.1 | Reagents and Materials

Sodium hydroxide, sulfuric acid, sodium chloride, potassium chloride, potassium dihydrogen phosphate, tris(hydroxymethyl) aminomethane (tris), and magnesium chloride solution (1 M) were purchased from Fisher scientific (Pittsburgh, PA, US). Ethylenediaminetetraacetic acid (EDTA), 6-Mercapto-1-hexanol, tris(2-carboxyethyl)phosphine (TCEP), phosphate-buffered saline tablets (working concentration of PBS 1x was 137 mM NaCl, 2.7 mM KCl, 10 mM $Na_2HPO_4$, 1.8 mM $KH_2PO_4$ pH 7.4), potassium ferrocyanide, and sodium hydrogen phosphate were purchased from Sigma Aldrich (St. Louis, MO, US). Potassium ferricyanide was purchased from Carlo Erba (Milan, Italy). Trastuzumab and human IgG were purchased from MCE MedChemExpress (Monmouth Junction, NJ, US), aliquoted and stored at +4 °C upon receipt until use. Ag/AgCl reference electrodes, platinum counter electrodes, and gold-plated electrode pin were purchased from CH Instruments (Austin, TX, US). Needles of different Gauge, 18–22, were purchased from BD (Franklin Lakes, NJ, US). Heparin was purchased from Sagent Pharmaceuticals (Schaumbur, IL, US). Gold wire 0.2 mm (0.008") diameter, platinum wire 0.125 mm (0.005") diameter and silver wire 0.125 mm (0.005") diameter were purchased from A-M Systems (Sequim, WA, US). Heat shrink tubing, Tw polyolefin, for in vitro sensors was purchased from Raychem (Menlo Park, CA, US). Heat shrink tubing, PTFE Sub-Lite-Wall black opaque, 0.5 mm (0.02") diameter, for in vivo sensors was purchased from Zeus (Branchburg Township, NJ, US). Steel cannula with a screw-type connector was purchased from Plastics One (Roanoke, VA, US). Silastic tubing (11 cm, i.d. 0.64 mm, o.d. 1.19 mm) was purchased from Dow Corning (Midland, MI, US). Sterile 6–0 silk suture was purchased from Fine Science Tools (Foster City, CA, US). Bovine blood in heparin (3 IU/mL) was obtained from HemoStat Laboratories (Dixon, CA, USA), and it was used as received.

### 4.2 | Animals

In vivo measurements were performed in male Sprague–Dawley rats (4–6 months old) purchased from Charles River Laboratories (Santa Cruz, CA), weighing between 300 and 500 g. All animals were pair housed in a standard light cycle room (08:00 on, 20:00 off) and allowed ad libitum access to food and water.

### 4.3 | Oligonucleotides

Oligos were purchased as dual-HPLC purification grade with a corresponding modification on the 3′ terminus and 5′ terminus from Biomers.net GmBH (Ulm, Germany) and Integrated DNA Technologies (Coralville, IA, USA). For sensor fabrication the aptamer variants were purchased modified with a thiol-C6-SS group at their 3′ end, and a methylene blue (MB) attached by a six-carbon linker to an amine at their 5′ end. The oligonucleotides were dissolved in TE buffer (10 mM Tris buffer, 1 mM EDTA, pH 7.8) at a concentration of 100 μM and then aliquoted and stored at −20 °C. The final concentrations of the oligonucleotides were confirmed using a Beckman Coulter DU 800 Spectrophotometer (Männedorf, Switzerland) using a 100 μL quartz cuvette and measuring the relative absorbance at 260 nm.

| DNA scaffold sensor | | | |
|---|---|---|---|
| **Oligo** | **5′** | **Sequence** | **3′** |
| Anchoring sequence | C6-SS | GGTTACAGATTACAACTAACC | MB |
| No linker | None | GTCCAGGGTTCCAAGGTGCTTCGTGGAC GGTTAGTTGTAATCTGTAACC | None |
| Poly T linker | None | GTCCAGGGTTCCAAGGTGCTTCGTGGAC TTTTTTGGTTAGTTGTAATCTGTAACC | None |
| Triethylene glycol linker | None | GTCCAGGGTTCCAAGGTGCTTCGTGGAC-iSp9-GGTTAGTTGTAATCTGTAACC | None |



26884062, 2026, 7, Downloaded from https://onlinelibrary.wiley.com/doi/10.1002/sstr.70539 by CochraneItalia, Wiley Online Library on [22/10/2026]. See the Terms and Conditions (https://onlinelibrary.wiley.com/terms-and-conditions) on Wiley Online Library for rules of use; OA articles are governed by the applicable Creative Commons License

| Electrochemical aptamer-based (EAB) sensor | | | |
|---|---|---|---|
| **Oligo** | **5′** | **Sequence** | **3′** |
| Parent Trunc 1 | C6-SS | GTGTCCAGGGTTCCAAGGTGCTTCGTGGACAC | MB |
| Trunc 2 | C6-SS | GTCCAGGGTTCCAAGGTGCTTCGTGGAC | MB |
| Trunc 2 (TA) | C6-SS | GTTCAGGGTTCCAAGGTGCTTCGTGAAC | MB |
| Trunc1 stem | C6-SS | **CTGAATCGAGA**GTGTCCAGGGTTCCAAGGTGCTTCGTGGA C AC TCT**CGATTCAG** | MB |

| Binding affinity assays in microscale thermophoresis (MST) | | | |
|---|---|---|---|
| **Oligo** | **5′** | **Sequence** | **3′** |
| Parent (Trunc1) | Cy5 | GTGTCCAGGGTTCCAAGGTGCTTCGTGGACAC | None |

For all the sequences above the bases in bold represent the stem portion and the underlined bases represent the TA base pair introduced in aptamer variant.

### 4.4 | Equipment and Instruments

Electrochemical measurements in vitro and in vivo were performed using a CH1000C multi-potentiostat from CH Instruments (Austin, TX, US). EIS measurements were performed using a PalmSens 4 potentiostat from PalmSens (Houten, Netherland). Binding affinity assays were performed using a MST Monolith NT.115 p instrument from Nanotemper Technologies GmbH (Munich, Germany). Sensor response characterization experiments at 37°C were performed in a temperature-controlled bath from Lauda–Brinkmann (Delran, NJ, US). Syringe pump (model KDS 200) was purchased from KD Scientific Inc. (Holliston, MA, US).

### 4.5 | NUPACK Simulations

We used NUPACK (http://www.nupack.org/) to predict the folding free energies of the re-engineered aptamer variants (Figure S1). 1 The aptamer sequences were analyzed by the software using the following parameters: (a) temperature: 25 °C; (b) number of strand species: 1; (c) maximum complex size: 4; (d) oligo concentration = 500 nM; in advanced options; (e) $[Na^+] = 0.137$ M, $[Mg^{2+}] = 0.02$ M; (f) dangle treatment: some.

### 4.6 | In Vitro Sensor Fabrication

We hand fabricated gold wire working electrodes using 200 μm diameter gold wire cut to a length of 4.5 cm, soldered into a gold-plated electrode pin (CH Instruments, Inc.) with 60/40 lead–selenium solder. We insulated 3.4 cm of each wire electrode with polyolefin heat-shrink 0.356 mm expanded inside diameter to 0.178 mm recovered inside diameter, by applying a heat gun at 180 °C. We cut the remaining exposed gold to a 6 mm working length by using a digital caliper and surgical scalpel blade. Finally, we further insulated the junction between the gold wire and the electrode pin with a modified thermoplastic liquid connector coating. To fabricate the sensors, we first electrochemically clean the gold surface of the working electrodes using external Ag/AgCl reference and Pt counter following the established protocol [53, 54]. In brief, we removed any residual thiol/organic contaminants on the electrode surface by (1) cycling the potential 1000 times between −1 and −1.6 V (all potentials reported relative to Ag/AgCl) in a solution of 0.5 M NaOH at 1 $Vs^{-1}$; then we rinsed electrodes and performed (2) cyclic voltammetry (CV) scans in 0.5 M $H_2SO_4$ at a potential window from 0 to 1.8 V and a scan rate of 1 $Vs^{-1}$ for 100 cycles. Then to increase microscopic surface area in the electrodes (and thus the signaling current) [44] we applied pulsing between 0 and 2 V for 16,000 cycle with a pulse length of 0.02 s in 0.5 M $H_2SO_4$. To reduce the disulfide bond on the aptamer before deposition we added 7 μL of 10 mM Tris (2-carboxyethyl) phosphine (TCEP) to 1 μL of the DNA-aptamer at 100 μM and incubated for 1 h in the dark at room temperature. We next adjusted the concentration of the reduced DNA to 500 nM (based on its absorbance at 260 nm) using PBS. For the DNA scaffold sensor the two DNA strands (1:1 ratio, 500 nM of Anchoring sequence and 500 nM of No linker or Poly T linker or Triethylene glycol linker) were hybridized for 1 h and we then immersed freshly cleaned gold electrodes in this aptamer solution for 1h at room temperature. For the Aptamer-based (EAB) sensor the 500 nM aptamer solution was directly immersed in freshly cleaned gold electrodes for 1h at room temperature. Next, we rinsed the electrodes with deionized water, and then incubated them in 10 mM 6-mercapto-1-hexanol solution in PBS overnight at 4°C protected from the light. We rinsed the sensors with deionized water before their use in measurements.

### 4.7 | In Vitro Measurements

We performed the electrochemical measurements using a CHI1000C potentiostat. We placed the sensors, secured through a Teflon cap, into an electrochemical cell containing the working buffer. For in vitro characterizations, we used external counter and Ag/AgCl reference macro electrodes, common for all the sensors measured in the cell. To characterize the SWV frequency dependence of the scaffold and aptamer-based sensors' signal gain (relative signal change when challenged with the saturating



26884062, 2026, 7, Downloaded from https://onlinelibrary.wiley.com/doi/10.1002/sstr.70539 by CochraneItalia, Wiley Online Library on [22/10/2026]. See the Terms and Conditions (https://onlinelibrary.wiley.com/terms-and-conditions) on Wiley Online Library for rules of use; OA articles are governed by the applicable Creative Commons License

target; Figures 2B and 3B), at least three sensors in the absence and presence of a saturating concentration of the trastuzumab (300 nM) were interrogated. We performed measurements at different frequencies ranging between 5 and 1000 Hz. The estimated peak currents in the absence of the target correspond to $Signal_0$ values, while those estimated in the presence of the target correspond to $Signal_i$. These raw current values were converted to relative signal change using the approach described in Equation (1) below, for each SWV frequency tested. Experimental binding curves were obtained experimentally in 3 mL of PBS (Figures 2C, 3C, and 4B) or in 3 mL of bovine whole blood (Figures 4A,C, S5, and S6) using at least three gold wire electrodes modified with the scaffold or aptamer variants. Specifically, in the absence of the target or interferents, SWV scans were collected (−0.15 to −0.45 V, 25 mM amplitude) at 100 Hz until the sensor's signal stabilized. We performed the titrations by sequentially making additions of trastuzumab or interferent to reach each target concentration. After each addition, we performed mixing by pipetting up and down the content of the electrochemical cell and waiting 10 min for stabilization. Measurements in phosphate-buffered saline were performed at room temperature (25 °C) or body temperature (37 °C). For the DNA-scaffold sensors the SWV signals were collected using a frequency of 300 Hz for the no linker variant, and 5 Hz for the poly T and triethylene glycol linker variants (Figure 2C). For the aptamer sensors the SWV signals were collected at frequencies of 10 Hz for the parent Trunc1 variant, 15 Hz for the Trunc1 stem variant, and 200 Hz for the Trunc2 and Trunc2(TA) variants (Figures 3C and 4B). For the binding curves obtained in undiluted bovine whole blood the SWV signals were collected at 60 Hz for the Trunc1 stem variant, and at 200 Hz for the Trunc2 and Trunc2(TA) variants (Figures 4A,C and S5). The peak current of the scaffold and aptamer sensors in the absence of the target, and at each target concentration, was extracted using a recently published script written in Python that analyzes the voltametric data by subtracting the baseline current from the peak maximum [55]. The raw peak current of each sensor was converted into the relative signal change (% Signal change) using the following equation:

$$\%\ \text{Signal change} = \frac{\text{Signal}_i - \text{Signal}_0}{\text{Signal}_0} \quad (1)$$

where $Signal_i$ is the peak signal of the square wave voltammogram at the given target concentration and $Signal_0$ the peak signal seen in absence of target. We fit our binding curves to Langmuir isotherms:

$$\text{Signal change} = \text{SC}_{\text{min}} + \frac{[\text{Trastuzumab} \cdot (\text{SC}_{\text{max}} - \text{SC}_{\text{min}})]}{(\text{Trastuzumab} + K_{\text{d}})} \quad (2)$$

where Signal change is the relative signal change measured by SWV (as described in Equation (1)), $SC_{min}$ the relative signal change seen in the absence of target, $SC_{max}$ the relative signal change seen at saturating target, $K_d$ the dissociation constant of the aptamer, and Trastuzumab is the concentration of trastuzumab. Continuous monitoring of Trunc2 sensor in vitro (Figure 4E,F) was obtained using the above experimental approach, with interrogation of the sensor at 400 Hz every 0.5 s at 25 and 37 °C in in undiluted bovine whole blood.

### 4.8 | Rat Blood Collection

Blood was collected from a single 460 g adult Sprague–Dawley rat (Charles River Laboratory, Santa Cruz, CA) to calibrate the sensor for in vivo experiments (Figure S12). The rat was allowed to acclimatize to the colony for at least 1 week. For collection, the animal was placed under anesthesia using isoflurane gas and, following abolishment of toe pinch response, a horizontal incision was made below the rib cage. The incision was extended on each side to under the front legs, at which point vertical incisions were made through the rib cage. The diaphragm was then cut to reveal the heart and the septum was pinned back using homeostats. A 20 mL syringe was prepared with 300 units of heparin in order to achieve a final concentration range of 20 units/mL. An 18G needle was attached to the top of the syringe and inserted into the left ventricle for blood collection. Very light pressure was applied to the syringe to facilitate blood removal. The blood draw (∼15 mL) was stopped when the flow of blood into the syringe finished, after which point the animal was euthanized via isofluorane overdose and confirmed with decapitation.

### 4.9 | In Vivo Sensor Fabrication

We fabricated and modified the electrodes following previously reported procedures [53, 54, 56]. A step-by-step photographic representation of the fabrication workflow is provided (Figure S8). Briefly, we cut the 7.75 cm segments of gold (all of them 0.2 mm diameter). We insulated each wire with heat-shrinkable PTFE tubing (HS Sub-Lite-Wall, 0.02 in, black opaque) leaving approximately 6 mm exposed gold to form the working electrode, and 6 mm of exposed silver and platinum to form the reference and counter electrodes (Figure S8A,B). The opposite ends of the wires were left exposed to allow electrical connections. We then bundled these together in PTFE tubing, with the end of each wire exposed (as shown in Figure 5B in the main text), leaving a gap of 1 mm gap between each wire's exposed area (Figure S8C). Finally, we trimmed the exposed wires, so the working electrode was 4 mm long and the reference and counter to 5 mm long, with the latter two being longer than the working electrode to ensure good electrochemical signaling. To convert the silver wires into a suitable reference, we immersed them in sodium hypochlorite (commercial bleach purchased in the local store) overnight to form a silver chloride film. Following the assembly and silver chloride layer formation, we converted the gold surface into an EAB sensor using the established protocol [53, 54, 56]. In brief, we performed an electrochemical cleaning using external reference and counter electrodes, immersing just the gold working electrode into the cleaning solutions, and keeping the reference and counter wires in the air to preserve the AgCl layer from the solutions. To remove any residual thiol/organic contaminants on the electrode surface, we started (1) cycling the potential 1000 times between −1 and −1.6 V (all potentials reported relative to Ag/AgCl) in a solution of 0.5 M NaOH at 1 $V \cdot s^{-1}$; then we rinsed electrodes and perform (2) pulsing between 0 and 2 V for 16 000 cycles with a pulse length of 0.02 s in 0.5 M $H_2SO_4$ to increase microscopic surface area in the electrodes (and thus the signaling current) [44]. To confirm the increase in electroactive surface area, cyclic voltammetry was performed before and after the roughening step by scanning the wire electrodes at 0.1 $V \cdot s^{-1}$ in 0.05 M $H_2SO_4$ between 0 and 1.8 V for eight cycles



26884062, 2026, 7, Downloaded from https://onlinelibrary.wiley.com/doi/10.1002/sstr.70539 by CochraneItalia, Wiley Online Library on [22/10/2026]. See the Terms and Conditions (https://onlinelibrary.wiley.com/terms-and-conditions) on Wiley Online Library for rules of use; OA articles are governed by the applicable Creative Commons License

(Figure S9). The increase in the reduction peak corresponding to chemisorbed oxygen on gold was used as an indicator of enhanced microscopic surface area. To reduce the disulfide bond on the aptamer before deposition, we added 7 µL of 10 mM Tris (2-carboxyethyl) phosphine (TCEP) to 1 µL of the DNA-aptamer at 100 µM and incubated for 1 h in the dark at room temperature. We next adjusted the concentration of the reduced DNA to 500 nM (based on its absorbance at 260 nm) using PBS. We then immersed freshly cleaned gold electrodes in this aptamer solution for 1h at room temperature. Next, we rinsed the electrodes with deionized water, and then incubated them in 10 mM 6-mercapto-1-hexanol solution in PBS overnight at 4 °C, protected from the light. We rinsed the sensors with deionized water before their use in measurements.

### 4.10 | In Vivo Sensor Characterization by Cyclic Voltammetry and EIS

We performed an electrochemical characterization of the gold wire electrode during the different steps of its modification using external reference and counter electrodes. First, we immersed the in vivo sensors in in PBS at pH 7.4 at room temperature before and after electrochemical cleaning and roughening (Figure S10A). Then, successful immobilization of the methylene blue–labeled aptamer was verified by cyclic voltammetry immersing the in vivo sensors in PBS at pH 7.4 at room temperature. The potential was scanned between −0.10 and −0.45 V (vs. Ag/AgCl) at a scan rate of 100 mV $s^{-1}$. Four consecutive scans were recorded for each electrode without prior equilibration. The resulting voltammograms display the characteristic redox peaks of methylene blue, confirming successful aptamer attachment (Figure S10B). We further characterized the sensor's surface modification through electrochemical impedance spectroscopy (EIS) measurements, carried out in 10 mM PBS (pH 7.4) containing 10 mM $[Fe(CN)_6]^{3-/4-}$ as the redox probe (Figure S11). The impedance spectra were recorded at a biased potential ($E_{DC}$) of 0.22 V (vs. Ag/AgCl) with a superimposed sinusoidal perturbation ($E_{AC}$) of 10 mV. An equilibration time of 10 s was applied before acquisition. The measurements were performed within a frequency range from 100 kHz to 0.1 Hz (10 points per decade). The Nyquist plots illustrate the effectiveness of the cleaning process (Figure S11A) and the sequential surface modifications (Gold, Gold+Apta, and Gold+Apta+MCH) (Figure S11B).

### 4.11 | In Vivo Measurements and Surgery

For in vivo experiments, we prepared our sensors by inserting the wire bundle into a 22-gauge catheter that has ∼2 mm windows cut into the catheter wall to expose the platinum and AgCl wires. To prevent air bubbles in the catheter, a syringe with a 27-gauge needle was used to fill the syringe with PBS: Once filled, we inserted the syringe into a PBS-containing electrochemical cell and collected a cyclic voltammogram (−0.1 to −0.5 V) to confirm the presence of the aptamer and proper functioning of the wire reference and counter in the sensor. We surgically inserted the sensor-catheter assembly into the right jugular vein of a Sprague Dawley rat as described previously [44, 47, 53]. Briefly, we shaved the chest area above the right and left jugular veins and cleaned the skin using betaine and 70% ethanol. We anesthetized the rat using 4% isofluorane in a plexiglass anesthesia chamber and then maintained 2–3% isofluorane/oxygen anesthesia through the experiment using a nose cone.

To enable the delivery of trastuzumab, we installed a silastic catheter and infusion line into the left jugular vein as previously described [53] using a steel cannula with a screw-type connector and silastic tubing (11 cm, i.d. 0.64 mm, o.d. 1.19 mm). We secured both EAB sensor and infusion lines tied into place with sterile 6–0 silk suture. Prior to any measurement or drug infusion, we manually infused into the rat 30 units of heparin. We then connected the infusion line to a syringe of trastuzumab (5 mg/mL trastuzumab and 200 units heparin/mL in filtered PBS) positioned on a syringe pump. Using alligator clips, we connected the sensor to the potentiostat. To confirm sensor connection and proper functioning, we first collected cyclic voltammograms and baselines SWV at 20 and 200 Hz. Then, we plotted and analyzed the square wave voltammograms in real time using a previously reported Python script8. After collecting a 15–30 min baseline, we used the syringe pump to inject the corresponding dose of trastuzumab (either 2 or 4 mg kg-1) at an infusion rate of 0.170 mL $min^{-1}$. The Python script [55] used to plot data in real time also processes the voltammograms applying a Savitzky–Golay smoothing filter and extracts the peak heights and calculates KDM values for the given frequencies, generating a text file containing the data.

### 4.12 | In Vivo Drift Correction

For the in vivo measurements, we selected two measuring frequencies, 20 and 200 Hz, to perform Kinetic differential measurement (KDM) for correction of the signal drift [42, 53, 57], we encounter when measuring in undiluted blood and in in vivo measurements:

$$\mathrm{KDM}\,(\%) = \mathrm{signal\,on}_{200\,\mathrm{Hz}} - \mathrm{signal\,off}_{20\,\mathrm{Hz}} \tag{3}$$

where KDM (%) is the resulting value of sensor signal after drift correction. Signal $\mathrm{on}_{200\,\mathrm{Hz}}$ is the % signal change obtained at 200 Hz and signal $\mathrm{off}_{20\,\mathrm{Hz}}$ is the % signal change obtained at 20 Hz.

### 4.13 | Animal Procedure Ethics

All animal procedures were consistent with the guidelines of the NIH Guide for Care and Use of Laboratory Animals (eighth edition, National Academy Press, 2011) and approved by the Institutional Animal Care and Use Committee (IACUC) of the University of California Santa Barbara (Ethics Approval Protocol Number 824). Dawley rats weighed 460 – 680 g and were pair-housed in a 12:12 standard light cycle room with ad libitum access to food and water as well as standard cage enrichment.

### 4.14 | $C_{max}$ from Pharmacokinetics In Vivo Data

The peak concentration ($C_{max}$) was directly obtained from the experimental values of trastuzumab concentration-time curves, by averaging the few points that conform the plateau after the spike of the injection of the drug.



26884062, 2026, 7, Downloaded from https://onlinelibrary.wiley.com/doi/10.1002/sstr.70539 by CochraneItalia, Wiley Online Library on [22/10/2026]. See the Terms and Conditions (https://onlinelibrary.wiley.com/terms-and-conditions) on Wiley Online Library for rules of use; OA articles are governed by the applicable Creative Commons License

### 4.15 | Binding Assays with MST

MST was used to quantify the binding affinity between the trastuzumab-binding aptamer and its target. Measurements were performed on a Monolith NT.115 p instrument (NanoTemper Technologies GmbH, Germany) at 25 °C. The Cy5-labeled aptamer was maintained at a constant concentration of 1 nM, while trastuzumab was titrated in a series of dilutions covering a concentration range from 0.03 nM to 1 μM. All samples were prepared in PBS buffer supplemented with 2 mM $Mg^{2+}$. Individual reaction mixtures (500 μL total volume) containing the labeled aptamer and the varying concentrations of the target were incubated in the dark at room temperature for 40 min to ensure binding equilibrium. Following incubation, the samples were loaded into standard MST capillaries (NanoTemper). The instrumental parameters were set to 40% excitation power and "medium" MST power. Data analysis and curve fitting were performed using the MO.Affinity Analysis software (NanoTemper), applying a 1: Langmuir binding model to determine the dissociation constant ($K_D$). The error values reported for dissociation constant ($K_D$) represent the standard error of the fit.

#### Author Contributions

**Alejandro Chamorro-Garcia:** conceptualization, methodology, investigation, writing – original draft and review & editing. **Lisa Fetter:** methodology and investigation. **Nicole A. Emmons:** methodology and investigation. **Myriam Alfonsini:** methodology and investigation. **Elisa Paialunga:** methodology, investigation and review & editing. **Bettina Glahn-Martínez:** methodology and investigation. **Elena Benito-Peña:** funding acquisition, methodology and investigation. **Giovanni Valenti:** conceptualization, funding acquisition, methodology, investigation, resources and review & editing. **Alessandro Porchetta:** funding acquisition, resources and review & editing. **Tod E. Kippin:** conceptualization, funding acquisition, writing – original draft and review & editing. **Kevin W. Plaxco:** conceptualization, funding acquisition, writing – original draft and review & editing. **Andrea Idili:** conceptualization, funding acquisition, methodology, investigation, supervision, writing – original draft and review & editing.

#### Acknowledgments

The research leading to these results has received funding from AIRC under MFAG 2024 - ID. 30591 project – P.I. Idili Andrea. This research has received funding from the European Union - NextGenerationEU under the program YOUNG RESEARCHER - MSCA (Project ID: MSCA_0000010) awarded by the Italian Ministerio dell'Università e della Ricerca (MUR) within the PNRR framework. NanoImmunoERA project has received funding from the European Union's MSCA Staff exchange Horizon Europe programme Grant Agreement No. 101086341. A.P. acknowledges funding from the Italian Ministry of University and Research (Project of National Interest, PRIN, 2022FPYZ2N). B.G.M. acknowledges funding from the Spanish Ministry of Science and Innovation through program PID2021-127457OB-C21. N.A.E. acknowledges funding from the Department of Defense through the National Defense Science and Engineering Graduate Fellowship.

#### Funding

This work was supported by the Associazione Italiana per la Ricerca sul Cancro (AIRC) under MFAG 2024 (Project ID 30591, P.I. Andrea Idili), European Union – NextGenerationEU under the YOUNG RESEARCHER – MSCA Program (Project ID: MSCA_0000010), Italian Ministry of University and Research (MUR) within the PNRR framework, European Union's Horizon Europe MSCA Staff Exchange Programme (Grant Agreement No. 101086341), Italian Ministry of University and Research (PRIN 2022, Project 2022FPYZ2N), Spanish Ministry of Science and Innovation (PID2021-127457OB-C21), and Department of Defence through the National Defense Science and Engineering Graduate Fellowship.

#### Ethics Statement

All animal procedures were consistent with the guidelines of the NIH Guide for Care and Use of Laboratory Animals (eighth edition, National Academy Press, 2011) and approved by the Institutional Animal Care and Use Committee (IACUC) of the University of California Santa Barbara (Ethics Approval Protocol Number 824). Dawley rats weighed 460–680 g and were pair-housed in a 12:12 standard light cycle room with ad libitum access to food and water with standard homecage environmental enrichment.

#### Conflicts of Interest

The authors declare no conflicts of interest.

#### Data Availability Statement

The data supporting the findings of this study are openly available in AMS Acta at https://amsacta.unibo.it/id/eprint/8868 DOI: 10.6092/unibo/amsacta/8868.

#### References

1. M. S. Castelli, P. McGonigle, and P. J. Hornby, "The Pharmacology and Therapeutic Applications of Monoclonal Antibodies," *Pharmacology Research & Perspectives* 7 (2019): 1–11, https://doi.org/10.1002/prp2.535.

2. S. Paul, M. F. Konig, D. M. Pardoll, et al., "Cancer Therapy With Antibodies," *Nature Reviews Cancer* 24 (2024): 399–426, https://doi.org/10.1038/s41568-024-00690-x.

3. A. M. Scott, J. P. Allison, and J. D. Wolchok, "Monoclonal Antibodies in Cancer Therapy," *Cancer Immunity* 12 (2012): 14.

4. S. Jin, Y. Sun, X. Liang, et al., "Emerging New Therapeutic Antibody Derivatives for Cancer Treatment," *Signal Transduction and Targeted Therapy* 7 (2022): 39, https://doi.org/10.1038/s41392-021-00868-x.

5. K. L. Gill, K. K. Machavaram, R. H. Rose, and M. Chetty, "Potential Sources of Inter-Subject Variability in Monoclonal Antibody Pharmacokinetics," *Clinical Pharmacokinetics* 55 (2016): 789–805, https://doi.org/10.1007/s40262-015-0361-4.

6. V. A. Thomas and J. P. Balthasar, "Understanding Inter-Individual Variability in Monoclonal Antibody Disposition," *Antibodies* 8 (2019): 56, https://doi.org/10.3390/antib8040056.

7. E. Chatelut, J. J. M. A. Hendrikx, J. Martin, J. Ciccolini, and D. J. A. R. Moes, "Unraveling the Complexity of Therapeutic Drug Monitoring for Monoclonal Antibody Therapies to Individualize Dose in Oncology," *Pharmacology Research & Perspectives* 9 (2021): 1–10, https://doi.org/10.1002/prp2.757.

8. L. Liu, "Pharmacokinetics of Monoclonal Antibodies and Fc-Fusion Proteins," *Protein & Cell* 9 (2018): 15–32, https://doi.org/10.1007/s13238-017-0408-4.

9. A. H. Conney, E. J. Pantuck, C. B. Pantuck, et al., "Variability in Human Drug Metabolism," in *Clinical Pharmacology & Therapeutics* (Palgrave Macmillan UK, 1980), 51–62, https://doi.org/10.1007/978-1-349-05952-2_5.

10. C. E. Knezevic, and W. Clarke, "Cancer Chemotherapy: The Case for Therapeutic Drug Monitoring," *Therapeutic Drug Monitoring* 42 (2020): 6–19, https://doi.org/10.1097/FTD.0000000000000701.

11. A. Bensalem and D. Ternant, "Pharmacokinetic Variability of Therapeutic Antibodies in Humans: A Comprehensive Review of Population Pharmacokinetic Modeling Publications," *Clinical Pharmacokinetics* 59 (2020): 857–874, https://doi.org/10.1007/s40262-020-00874-2.



26884062, 2026, 7, Downloaded from https://onlinelibrary.wiley.com/doi/10.1002/sstr.70539 by CochraneItalia, Wiley Online Library on [22/10/2026]. See the Terms and Conditions (https://onlinelibrary.wiley.com/terms-and-conditions) on Wiley Online Library for rules of use; OA articles are governed by the applicable Creative Commons License

12. A. S. Strik, Y.-M. C. Wang, L. E. Ruff, W. Yashar, B. T. Messmer, and D. R. Mould, "Individualized Dosing of Therapeutic Monoclonal Antibodies—a Changing Treatment Paradigm?," *AAPS Journal* 20 (2018): 99, https://doi.org/10.1208/s12248-018-0257-y.

13. H. Liang, L. Zhou, P. Chen, et al., "Optical Microfiber with a Gold Nanorods–Black Phosphorous Nanointerface: An Ultrasensitive Biosensor and Nanotherapy Platform," *Analytical Chemistry* 94 (2022): 8058–8065, https://doi.org/10.1021/acs.analchem.2c01499.

14. M. A. Booth, M. K. Erdal, M. Larson, et al., "Pilot Phase Clinical Trial of a Wearable, Electrochemical Aptamer-Based Patch for Continuous Drug Concentration Measurement," *Nature Biotechnology* (2026), https://doi.org/10.1038/s41587-026-03010-w.

15. K. J. Cash, F. Ricci, and K. W. Plaxco, "An Electrochemical Sensor for the Detection of Protein–Small Molecule Interactions Directly in Serum and Other Complex Matrices," *Journal of the American Chemical Society* 131 (2009): 6955–6957, https://doi.org/10.1021/ja9011595.

16. A. Papachristos, P. Kemos, H. Kalofonos, and G. Sivolapenko, "Correlation Between Bevacizumab Exposure and Survival in Patients with Metastatic Colorectal Cancer," *Oncologist* 25 (2020): 853–858, https://doi.org/10.1634/theoncologist.2019-0835.

17. O. Kolesova, F. Tomassetti, P. Cerini, et al., "Evaluation of ECLIA Antigen Detection Tests as Screening Methods for COVID-19 in Comparison with Molecular Analysis," *Irish Journal of Medical Science* 191 (2022): 2213–2217, https://doi.org/10.1007/s11845-021-02863-1.

18. C. K. Imamura, "Therapeutic Drug Monitoring of Monoclonal Antibodies: Applicability Based on Their Pharmacokinetic Properties," *Drug Metabolism and Pharmacokinetics* 34 (2019): 14–18, https://doi.org/10.1016/j.dmpk.2018.11.003.

19. M. Ovacik and K. Lin, "Tutorial on Monoclonal Antibody Pharmacokinetics and Its Considerations in Early Development," *Clinical and Translational Science* 11 (2018): 540–552, https://doi.org/10.1111/cts.12567.

20. S.-L. Wang, L. Ohrmund, S. Hauenstein, et al., "Development and Validation of a Homogeneous Mobility Shift Assay for the Measurement of Infliximab and Antibodies-to-Infliximab Levels in Patient Serum," *Journal of Immunological Methods* 382 (2012): 177–188, https://doi.org/10.1016/j.jim.2012.06.002.

21. A. P. F. Turner, "Biosensors: Sense and Sensibility," *Chemical Society Reviews* 42 (2013): 3184, https://doi.org/10.1039/c3cs35528d.

22. K. S. McKeating, A. Aubé, and J.-F. Masson, "Biosensors and Nanobiosensors for Therapeutic Drug and Response Monitoring," *Analyst* 141 (2016): 429–449, https://doi.org/10.1039/C5AN01861G.

23. Y. Xiao, R. Y. Lai, and K. W. Plaxco, "Preparation of Electrode-Immobilized, Redox-Modified Oligonucleotides for Electrochemical DNA and Aptamer-Based Sensing," *Nature Protocols* 2 (2007): 2875–2880, https://doi.org/10.1038/nprot.2007.413.

24. Y. Xiao, A. A. Lubin, A. J. Heeger, and K. W. Plaxco, "Label-Free Electronic Detection of Thrombin in Blood Serum by Using an Aptamer-Based Sensor," *Angewandte Chemie* 117 (2005): 5592–5595, https://doi.org/10.1002/ange.200500989.

25. P. G. Morris and C. A. Hudis, "Trastuzumab-Related Cardiotoxicity Following Anthracycline-Based Adjuvant Chemotherapy: How Worried Should We Be?," *Journal of Clinical Oncology* 28 (2010): 3407–3410, https://doi.org/10.1200/JCO.2009.26.0125.

26. K. Chen, J. Zhou, Z. Shao, et al., "Aptamers as Versatile Molecular Tools for Antibody Production Monitoring and Quality Control," *Journal of the American Chemical Society* 142 (2020): 12079–12086, https://doi.org/10.1021/jacs.9b13370.

27. C. Entzian and T. Schubert, "Studying Small Molecule–aptamer Interactions Using MicroScale Thermophoresis (MST)," *Methods* 97 (2016): 27–34, https://doi.org/10.1016/j.ymeth.2015.08.023.

28. P. Baaske, C. J. Wienken, P. Reineck, S. Duhr, and D. Braun, "Optical Thermophoresis for Quantifying the Buffer Dependence of Aptamer Binding," *Angewandte Chemie International Edition* 49 (2010): 2238–2241, https://doi.org/10.1002/anie.200903998.

29. D. Kang, C. Parolo, S. Sun, N. E. Ogden, F. W. Dahlquist, and K. W. Plaxco, "Expanding the Scope of Protein-Detecting Electrochemical DNA "Scaffold" Sensors," *ACS Sensors* 3 (2018): 1271–1275, https://doi.org/10.1021/acssensors.8b00311.

30. N. E. Ogden, M. Kurnik, C. Parolo, and K. W. Plaxco, "An Electrochemical Scaffold Sensor for Rapid Syphilis Diagnosis," *Analyst* 144 (2019): 5277–5283, https://doi.org/10.1039/C9AN00455F.

31. P. Dauphin-Ducharme and K. W. Plaxco, "Maximizing the Signal Gain of Electrochemical-DNA Sensors," *Analytical Chemistry* 88 (2016): 11654–11662, https://doi.org/10.1021/acs.analchem.6b03227.

32. Y. Tokuda, T. Watanabe, Y. Omuro, et al., "Dose Escalation and Pharmacokinetic Study of a Humanized Anti-HER2 Monoclonal Antibody in Patients with HER2/Neu-Overexpressing Metastatic Breast Cancer," *British Journal of Cancer* 81 (1999): 1419–1425, https://doi.org/10.1038/sj.bjc.6690343.

33. L. R. Schoukroun-Barnes, F. C. Macazo, B. Gutierrez, J. Lottermoser, J. Liu, and R. J. White, "Reagentless, Structure-Switching, Electrochemical Aptamer-Based Sensors," *Annual Review of Analytical Chemistry* 9 (2016): 163–181, https://doi.org/10.1146/annurev-anchem-071015-041446.

34. M. A. Pellitero, A. Shaver, and N. Arroyo-Currás, "Critical Review—Approaches for the Electrochemical Interrogation of DNA-Based Sensors: A Critical Review," *Journal of The Electrochemical Society* 167 (2020): 037529, https://doi.org/10.1149/2.0292003JES.

35. P. L. Mage, B. S. Ferguson, D. Maliniak, K. L. Ploense, T. E. Kippin, and H. T. Soh, "Closed-Loop Control of Circulating Drug Levels in Live Animals," *Nature Biomedical Engineering* 1 (2017): 0070, https://doi.org/10.1038/s41551-017-0070.

36. N. Arroyo-Currás, P. Dauphin-Ducharme, K. Scida, and J. L. Chávez, "From the Beaker to the Body: Translational Challenges for Electrochemical, Aptamer-Based Sensors," *Analytical Methods* 12 (2020): 1288–1310, https://doi.org/10.1039/D0AY00026D.

37. R. J. White and K. W. Plaxco, "Exploiting Binding-Induced Changes in Probe Flexibility for the Optimization of Electrochemical Biosensors," *Analytical Chemistry* 82 (2010): 73–76, https://doi.org/10.1021/ac902595f.

38. A. Idili, A. Amodio, M. Vidonis, J. Feinberg-Somerson, M. Castronovo, and F. Ricci, "Folding-Upon-Binding and Signal-On Electrochemical DNA Sensor with High Affinity and Specificity," *Analytical Chemistry* 86 (2014): 9013–9019, https://doi.org/10.1021/ac501418g.

39. A. L. Quartino, C. Hillenbach, J. Li, et al., "Population Pharmacokinetic and Exposure–response Analysis for Trastuzumab Administered Using a Subcutaneous "Manual Syringe" Injection or Intravenously in Women with HER2-Positive Early Breast Cancer," *Cancer Chemotherapy and Pharmacology* 77 (2016): 77–88, https://doi.org/10.1007/s00280-015-2922-5.

40. S. R. Khan, L. Chaker, M. A. Ikram, R. P. Peeters, P. M. van Hagen, and V. A. S. H. Dalm, "Determinants and Reference Ranges of Serum Immunoglobulins in Middle-Aged and Elderly Individuals: A Population-Based Study," *Journal of Clinical Immunology* 41 (2021): 1902–1914, https://doi.org/10.1007/s10875-021-01120-5.

41. D. Leveque, L. Gigou, and J. Bergerat, "Clinical Pharmacology of Trastuzumab," *Current Clinical Pharmacology* 3 (2008): 51–55, https://doi.org/10.2174/157488408783329931.

42. A. Chamorro-Garcia, M. Alfonsini, D. Caprioli, C. Parolo, and A. Idili, "Continuous Monitoring of Biomolecular Targets In Vivo Using DNA-Based Electrochemical Sensors," *Current Opinion in Electrochemistry* 54 (2025): 101765, https://doi.org/10.1016/j.coelec.2025.101765.

43. A. M. Downs, and K. W. Plaxco, "Real-Time, In Vivo Molecular Monitoring Using Electrochemical Aptamer Based Sensors: Opportunities



26884062, 2026, 7, Downloaded from https://onlinelibrary.wiley.com/doi/10.1002/sstr.70539 by CochraneItalia, Wiley Online Library on [22/10/2026]. See the Terms and Conditions (https://onlinelibrary.wiley.com/terms-and-conditions) on Wiley Online Library for rules of use; OA articles are governed by the applicable Creative Commons License

and Challenges," *ACS Sensors* 7 (2022): 2823–2832, https://doi.org/10.1021/acssensors.2c01428.

44. N. Arroyo-Currás, K. Scida, K. L. Ploense, T. E. Kippin, and K. W. Plaxco, "High Surface Area Electrodes Generated via Electrochemical Roughening Improve the Signaling of Electrochemical Aptamer-Based Biosensors," *Analytical Chemistry* 89 (2017): 12185–12191, https://doi.org/10.1021/acs.analchem.7b02830.

45. A. M. Downs, J. Gerson, K. K. Leung, K. M. Honeywell, T. Kippin, and K. W. Plaxco, "Improved Calibration of Electrochemical Aptamer-Based Sensors," *Scientific Reports* 12 (2022): 5535, https://doi.org/10.1038/s41598-022-09070-7.

46. J. D. Pham, L. C. Fetter, J. Gerson, T. E. Kippin, K. W. Plaxco, and K. K. Leung, "On the Blood Components Contributing to the Drift of Electrochemical Aptamer-Based Biosensors," *ACS Sensors* 10 (2025): 5160–5165, https://doi.org/10.1021/acssensors.5c01267.

47. A. Chamorro-Garcia, J. Gerson, C. Flatebo, et al., "Real-Time, Seconds-Resolved Measurements of Plasma Methotrexate In Situ in the Living Body," *ACS Sensors* 8 (2023): 150–157, https://doi.org/10.1021/acssensors.2c01894.

48. E. Verrinder, J. Gerson, K. Leung, T. E. Kippin, and K. W. Plaxco, "Dual-Frequency, Ratiometric Approaches to EAB Sensor Interrogation Support the Calibration-Free Measurement of Specific Molecules In Vivo," *ACS Sensors* 9 (2024): 3205–3211, https://doi.org/10.1021/acssensors.4c00516.

49. A. M. Dahlberg, L. M. Kaminskas, A. Smith, et al., "The Lymphatic System Plays a Major Role in the Intravenous and Subcutaneous Pharmacokinetics of Trastuzumab in Rats," *Molecular Pharmaceutics* 11 (2014): 496–504, https://doi.org/10.1021/mp400464s.

50. H.-Y. Chang, K. Morrow, E. Bonacquisti, W. Zhang, and D. K. Shah, "Antibody Pharmacokinetics in Rat Brain Determined Using Microdialysis," *mAbs* 10 (2018): 843–853, https://doi.org/10.1080/19420862.2018.1473910.

51. A. Shaver and N. Arroyo-Currás, "The Challenge of Long-Term Stability for Nucleic Acid-Based Electrochemical Sensors," *Current Opinion in Electrochemistry* 32 (2022): 100902, https://doi.org/10.1016/j.coelec.2021.100902.

52. K. Son, J. M. Gibson, J. Gerson, et al., "Continuous, Week-Long, Seconds-Resolved In Vivo Drug Measurements Performed with a Xenonucleic Acid-Employing Electrochemical, Aptamer-Based Sensor," *Journal of the American Chemical Society* 148 (2026): 10016, https://doi.org/10.1021/jacs.5c22605.

53. N. Arroyo-Currás, J. Somerson, P. A. Vieira, K. L. Ploense, T. E. Kippin, and K. W. Plaxco, "Real-Time Measurement of Small Molecules Directly in Awake, Ambulatory Animals," *Proceedings of the National Academy of Sciences* 114 (2017): 645–650, https://doi.org/10.1073/pnas.1613458114.

54. L. C. Fetter, M. H. McDonough, T. E. Kippin, and K. W. Plaxco, "Effects of Physiological-Scale Variation in Cations, pH, and Temperature on the Calibration of Electrochemical Aptamer-Based Sensors," *ACS Sensors* 9 (2024): 6675–6684, https://doi.org/10.1021/acssensors.4c02274.

55. S. D. Curtis, K. L. Ploense, M. Kurnik, et al., "Open Source Software for the Real-Time Control, Processing, and Visualization of High-Volume Electrochemical Data," *Analytical Chemistry* 91 (2019): 12321–12328, https://doi.org/10.1021/acs.analchem.9b02553.

56. Y. Wu and K. W. Plaxco, "On the Design, Fabrication, and Operation of Electrochemical Aptamer-Based Sensors," *ACS Sensors* 10 (2025): 7218–7230, https://doi.org/10.1021/acssensors.4c03465.

57. P. Dauphin-Ducharme, K. Yang, N. Arroyo-Currás, et al., "Electrochemical Aptamer-Based Sensors for Improved Therapeutic Drug Monitoring and High-Precision, Feedback-Controlled Drug Delivery," *ACS Sensors* 4 (2019): 2832–2837, https://doi.org/10.1021/acssensors.9b01616.

## Supporting Information

Additional supporting information can be found online in the Supporting Information section.



26884062, 2026, 7, Downloaded from https://onlinelibrary.wiley.com/doi/10.1002/sstr.70539 by CochraneItalia, Wiley Online Library on [22/10/2026]. See the Terms and Conditions (https://onlinelibrary.wiley.com/terms-and-conditions) on Wiley Online Library for rules of use; OA articles are governed by the applicable Creative Commons License